Partially carbonised carbon fibres as improved electrodes for structural battery applications

Downloaded from: https://research.chalmers.se, 2026-09-09 12:43 UTC

Citation for the original published paper (version of record):
Tavano, R., Randall, J., Le Thao, N. et al (2026). Partially carbonised carbon fibres as improved electrodes for structural battery applications. Communications Materials, 7(1). http://dx.doi.org/10.1038/s43246-026-01194-x

N.B. When citing this work, cite the original published paper.

research.chalmers.se offers the possibility of retrieving research publications produced at Chalmers University of Technology. It covers all kind of research output: articles, dissertations, conference papers, reports etc. since 2004. research.chalmers.se is administrated and maintained by Chalmers Library

(article starts on next page)

communications materials

A Nature Portfolio journal

Article

https://doi.org/10.1038/s43246-026-01194-x

Partially carbonised carbon fibres as improved electrodes for structural battery applications

Check for updates

Ruben Tavano [1] ✉, James D. Randall [2], Nguyen Nguyen Le Thao[2], Claudia Creighton[2], Johanna Xu [1], Luke C. Henderson [2] & Leif E. Asp [1] ✉

Carbon fibres are promising materials for structural battery anodes because they can simultaneously provide mechanical reinforcement and act as the electrochemically active material. Their performance depends strongly on their internal structure, which is influenced by the temperature used during carbonisation. Here, we show that partially carbonised carbon fibres produced at different maximum carbonisation temperatures (800 °C to 1100 °C) display systematic changes in both mechanical and electrochemical behaviour. Mechanical testing shows that increasing the carbonisation temperature leads to higher stiffness and tensile strength. Electrochemical measurements reveal a similar trend, with higher reversible capacity and improved cycling stability at higher temperatures. Thus, results show that the general antagonistic dependence on carbonisation temperature observed for conventional carbon fibres is not found for partially carbonised fibres. The partially carbonised fibres show up to 40 percent better electrochemical performance than conventional intermediate modulus carbon fibres. These results highlight the potential in the use of partially carbonised carbon fibres for next-generation structural battery composites, allowing for an expanded multifunctional design window.

The development of multifunctional materials is transforming energy storage technologies, especially for applications in transportation and portable electronics. Structural battery composites (SBCs) are a promising concept, combining mechanical strength with energy storage capability[1–3]. By allowing structural components to also store energy, SBCs can reduce overall system weight and improve energy efficiency. This is achieved using materials such as carbon fibres, which provide good mechanical properties while also allowing lithium-ion storage within their microstructure. Typically, SBCs are made from thin-ply carbon fibre tows that act as negative electrodes, stacked with separators and counter electrodes[2,4–9]. These assemblies are infused with a structural battery electrolyte (SBE), which contributes to both ionic movement and mechanical load transfer between the layers[10–15].

Although the mechanical behaviour of commercial carbon fibres is well established, due to their longstanding use in composite applications, their electrochemical characteristics remain highly underexplored. The use of carbon fibres as active material in lithium-ion battery negative electrodes was first explored in 1990[16]. This early investigation highlighted the critical relationship between carbon fibre microstructure and electrochemical behaviour. Building on this foundation, Snyder et al. demonstrated that carbon fibres derived from polyacrylonitrile (PAN) precursors exhibit superior lithium-ion intercalation properties compared to their pitch-based counterparts, with more than double the capacity at slow C-rates[17].

Studies by Jacques et al. and Duan et al. provided early insights into the effects of lithium insertion on the structural and mechanical integrity of these fibres[18–21]. Furthermore, Kjell et al. systematically evaluated the electrochemical performance of common PAN-based carbon fibres, while Hagberg et al. compared the lithiation behaviour of intermediate modulus (IM) fibres like T800 and IMS65 against high modulus (HM) variants such as M60J using precise coulometry analyses[22,23]. IM fibres generally delivered higher electrochemical capacities (with reversible capacities up to 140 mAh g^{-1}), although the reasons for this performance difference were not immediately evident. Fredi et al. utilised high-resolution transmission electron microscopy and in-situ Raman spectroscopy to uncover distinct lithiation behaviour among T800, IMS65, and M60J fibres[24]. Their results revealed that IM fibres displayed behaviour akin to amorphous carbon during lithium insertion, with unique lithiation signatures for each fibre type. In contrast, the HM fibre followed a more graphite-like staging

[1]Department of Mechanical Engineering, Chalmers University of Technology, Göteborg, Sweden. [2]Institute for Frontier Materials, Deakin University, Waurn Ponds, VIC, Australia. ✉e-mail: ruben.tavano@chalmers.se; leif.asp@chalmers.se

Table 1 | Physical properties for the partially carbonised carbon fibres, and comparison with FC and T800 fibres

Fibre type	Density [g cm^{-3}]	Fibre diameter [μm]	BET surface area [m^2 g^{-1}]	Electrical conductivity [S cm^{-1}]
T800[59]	1.800	5.00	0.52	714.34
FC	1.793	7.50	1.17	675.52
PC800	1.737	8.82	1.10	0.10
PC900	1.758	8.34	1.14	5.65
PC1000	1.765	8.15	1.02	63.09
PC1100	1.780	7.93	1.08	253.40

mechanism that was obstructed by structural defects within its large crystalline domains, ultimately limiting its lithium capacity. Johansen et al. extended this understanding by analysing the impact of nitrogen heteroatoms in the fibre microstructure[25]. They observed that IMS65 contained a higher proportion of pyridinic and pyrrolic nitrogen (20.5%) compared to T800 (14.2%). Since these nitrogen species tend to localise at defect sites and enhance lithium coordination, their elevated concentration in IMS65 likely contributed to its superior electrochemical performance compared to T800 fibres.

More recently, Asp et al. highlighted the potential of IM fibres in multifunctional applications by integrating a T800 fibre tow into a laminated SBC, where it served as the negative electrode[26]. The resulting prototype combined a specific energy of 24 Wh kg^{-1} with a tensile stiffness of 25 GPa, demonstrating effective dual functionality. Building on this, Chaudhary et al. developed the first all-fibre-based SBC using lithium iron phosphate-coated carbon fibres as the positive electrode[27,28]. This advancement enhanced the structural performance, delivering a tensile modulus of 76 GPa, albeit with a slight improvement in energy density, which reached 30 Wh kg^{-1}.

Despite these recent developments, several key challenges remain. Commercial carbon fibres have been optimised exclusively for mechanical performance, with no consideration for electrochemical properties. This situation is further complicated by limited transparency around proprietary production features, such as precursor chemistry and processing steps, and the widespread use of sizing agents, whose composition can significantly influence electrochemical performance[29,30].

To address these limitations, researchers, including Xu et al. and Tavano et al. have investigated customised carbon fibres made from the same PAN-based precursor, each introducing targeted variations in the production process[31,32]. Xu et al. altered the tension applied to the precursor fibre during the stabilisation step, while Tavano et al. focused on assessing the effects of different carbonisation temperature profiles. These controlled modifications enabled a systematic investigation into how processing affects multifunctional performance. Both studies revealed a fundamental trade-off: as electrochemical capacity improved, mechanical strength decreased. Specifically, fibres with a more disordered carbonaceous microstructure, featuring reduced graphitisation, smaller crystallite dimensions, and increased interlayer spacing, demonstrated superior lithium storage capabilities. This underscores a critical materials design challenge: optimisation of carbon fibre morphology to balance structural and electrochemical demands. Similar structure–property relationships have also been widely reported for carbon-based electrode materials, where graphitic ordering, defect density, and pore structure play a key role in determining lithium storage behaviour and electrochemical stability[33–35].

In the present work, we investigate a novel approach to carbon fibre manufacturing. For the first time in carbon fibre-based electrodes, a partial carbonisation is employed, resulting in a distinctly different microstructure with gradually varying properties[36]. With this processing route, we observe an inverse trend in which higher carbonisation temperatures correlate to an improvement in the electrochemical storage capacity alongside an increase in the mechanical performance. This strongly suggests the presence of a preferred temperature window that simultaneously maximises mechanical strength and electrochemical storage. Unlike previously studied HM and IM fibres, which prioritise tensile modulus or multifunctionality, respectively, partially carbonised fibres open new opportunities for structural battery applications where mechanical demands are modest, but energy storage is crucial. These fibres may represent a new class of multifunctional materials tailored for energy-centric applications within structural systems.

Results and discussion

In this study, we manufacture and analyse four different types of partially carbonised carbon fibres. These are labelled PC800, PC900, PC1000, and PC1100. Here, "PC" indicates the partially carbonised nature of the fibres, and the number indicates the maximum reached carbonisation temperature in degrees Celsius. For comparison purposes, the results for two IM carbon fibres investigated in previous studies are also reported. These include commercially available T800 carbon fibres, which are considered the state-of-the-art carbon fibres for structural battery negative electrodes, and the custom-made cool temperature profile (CP) fibres reported by Tavano et al. hereafter referred to as fully carbonised (FC) fibres[32]. Comparing the present fibres to the FC fibres is particularly relevant due to their nearly identical manufacturing processes. The only difference is an additional high-temperature carbonisation step at 1300 °C applied to the FC fibres, as used for other IM carbon fibres. This step introduces notable changes to the microstructure and fibre properties, which will be discussed in the coming sections.

Fundamental physical properties

Table 1 presents an overview of the fundamental physical properties of all the fibres in this study. A similar density to IM fibres is measured for all the partially carbonised fibres, with an increase in density from 1.737 g cm^{-3} for PC800 fibres to 1.780 g cm^{-3} for PC1100 fibres. This increase correlates with a 10% reduction in diameter from the lowest to the highest carbonisation temperature. The density is in the same range as IM fibres, while a larger diameter is measured for all partially carbonised fibres. This is likely linked to the initial precursor fibre diameter, and less to the maximum carbonisation temperature.

The BET surface area is consistent across all samples, with the exception of the T800 fibres. In this case, the value is around half that measured for the other fibres, probably due to the measurement being performed on sized fibres. A clear difference between the surface of the sized fibre and the unsized fibre was shown in previous studies[31,32,37]. Overall, these values are in the low surface area range, and no visible morphological differences can be observed from the SEM images presented in Fig. 1.

Electrical conductivity is essential for energy storage applications, as the active material must efficiently transport electrons to and from the current collector. A clear minimum conductivity threshold has not been established in the literature for structural battery applications. A large variation in measured electrical conductivity is observed for the partially carbonised fibres. Furthermore, compared to IM fibres, up to three orders of magnitude lower conductivity values are measured. From the lowest conductivity of the PC800 fibres, almost an order of magnitude increase is observed for each 100 °C increase in the maximum carbonisation temperature, from 0.1 to 253.4 S cm^{-1}.

Following the evaluation of physical properties, the carbon fibres were subjected to elemental analysis to determine atomic abundance ratios as a function of the manufacturing temperature profile. As shown in Table 2, carbon content rises progressively from 72.0% in PC800 to 84.7% in PC1100. This trend reflects the thermal removal of non-carbon elements. Accordingly, hydrogen and oxygen contents decrease steadily due to dehydrogenation and the elimination of oxygen-containing functional groups. Nitrogen also decreases from 18.5% at 800 °C to 11.9% at 1100 °C as denitrogenation reactions become more extensive. The FC sample carbonised at 1300 °C exhibits a further increase in carbon content (91.2%) and a corresponding reduction in hydrogen, nitrogen, and oxygen compared to

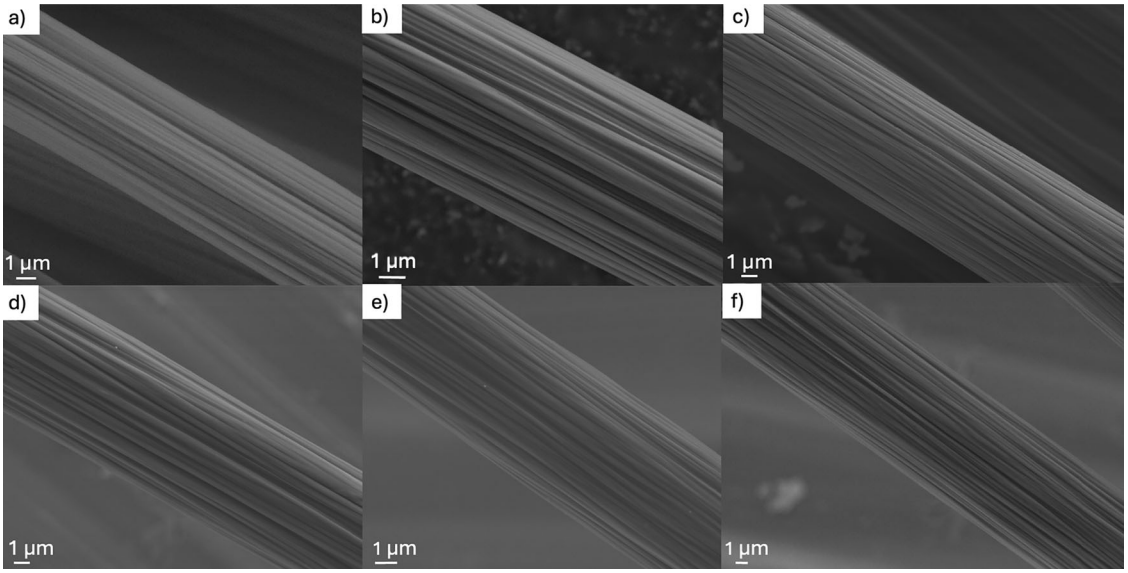

Fig. 1 | SEM images of the surface of the carbon fibres at ×10k magnification. **a** T800 fibres, **b** FC fibres from Tavano et al.[32], **c** PC800 fibres, **d** PC900 fibres, **e** PC1000 fibres and **f** PC1100 fibres.

Table 2 | Atomic composition in weight percentage for the manufactured partially carbonised fibres, and comparison with FC and T800 fibres

Fibre type	Carbon content [%]	Hydrogen content [%]	Nitrogen content [%]	Oxygen content [%]
T800[25,59]	>96.0	<0.8	1.2	2.0
FC	91.2	0.3	8.2	1.9
PC800	72.0	1.8	18.5	7.8
PC900	74.1	1.3	17.8	6.8
PC1000	76.8	1.0	15.8	6.4
PC1100	84.7	0.6	11.9	2.8

Table 3 | Data derived from the Raman spectra and their fits

Fibre type	D peak position (intensity) [cm^{-1}]	G peak position (intensity) [cm^{-1}]	I_D/I_G [–]	$HWHM_G$ [cm^{-1}]	L_a (TK) [nm]	L_a (ML) [nm]
T800	1350 (0.944)	1590 (1.000)	0.94	47.50	5.25	5.21
FC	1350 (0.950)	1590 (1.000)	0.95	48.50	5.22	5.00
PC800	1340 (1.000)	1570 (1.000)	1.25	56.50	3.98	3.30
PC900	1340 (1.000)	1570 (0.949)	1.18	55.00	4.20	3.62
PC1000	1350 (1.000)	1590 (0.846)	1.05	53.00	4.71	4.04
PC1100	1350 (0.998)	1590 (0.802)	1.00	52.50	4.97	4.15

In the crystallite length calculation, TK denotes the calculation using the ratio of I_D/I_G according to the Tuinstra–Koenig model, ML denotes the calculation using the HWHM according to the Mallet-Ladeira model.

PC1100, indicating continued aromatisation at higher temperatures. Although FC fibres show a significantly more carbon-rich composition than the partially carbonised fibres, their elemental content remains below that of commercial T800 fibres (>96% carbon content), reflecting that full graphitisation has not yet been achieved at 1300 °C.

Microstructural analysis

The carbonaceous microstructure of the fibres is characterised using Raman spectroscopy to identify any differences caused by the maximum temperature during manufacture. Differences in Raman spectra are observed, with different intensities of the D and G peaks along with differences in the Raman shift values.

The Raman analysis results are summarised in Table 3. Figure 2a presents the Raman spectra of all fibre samples in the 500–3500 cm^{-1} range. The inset in Fig. 2a highlights the D and G peaks. All samples display similar G′ peaks, indicative of a low degree of crystallinity, small domain sizes, and a turbostratic or amorphous carbon structure[38]. For the IM fibres (FC and T800), the D and G peak intensities are comparable, yielding intensity ratios of 0.95 and 0.94, respectively. This similarity suggests a comparable level of disorder, with the slightly higher ratio for the FC fibre likely due to a lower carbonisation temperature than that of the commercial T800 fibre. In contrast, all the partially carbonised fibres exhibit a notably higher D peak intensity, corresponding to a higher degree of disorder and a less graphitised structure. I_D/I_G ratios above 1.00 are obtained for all the partially carbonised fibres, with a decreasing trend from PC800 to PC1100 fibres. This indicates that an increase in the maximum carbonisation temperature leads to an increase in the graphitisation extent and crystalline order, as reflected by the increase in the G peak intensity. At the same time, a decrease in the D peak is observed for the same temperature increase. Using the Tuinstra–Koenig (TK) and the Mallet-Ladeira (ML) relations, an average crystallite length is calculated from the Raman spectra[39,40]. It should be noted that the Tuinstra–Koenig relation was originally formulated for graphitic carbons and loses validity for highly disordered materials. For the partially carbonised fibres in this study, which exhibit significant structural disorder, the Mallet-Ladeira relation, derived from a broader range of disordered carbons and based on the HWHM of the G peak rather than the I_D/I_G ratio, is therefore the more physically appropriate model and is used as the primary basis for discussion. Smaller crystallite sizes are obtained for lower carbonisation temperatures, with a 20% difference between PC800 and PC1100. Figure 2b shows that the D and G peaks for the PC800 and PC900 fibres are slightly red-shifted (i.e., shifted to lower Raman shifts) relative to other fibres. This shift may be attributed to residual microstructural strain from partial carbonisation and the presence of heteroatoms and increased structural disorder[24].

The results from the WAXS analyses are shown in Table 4. The WAXS analyses present a clear, temperature-dependent structural evolution for the manufactured fibres. The WAXS spectra along the equatorial direction (corresponding to [002] reflection) are shown in Fig. S1. The partially carbonised fibres show equatorial peak positions between 22.550° and

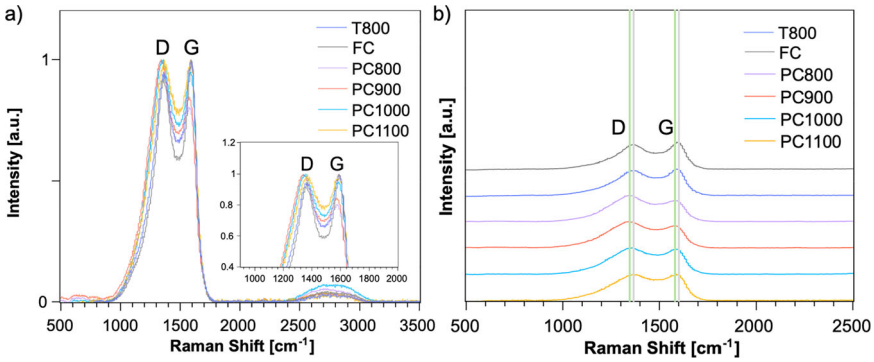

Fig. 2 | Raman spectra of the partially carbonised carbon fibres and comparison with FC and T800 fibres. a Full spectra with inset showing a magnified view of the characteristic D and G peaks. **b** Vertically shifted view of the spectra shows a red-shift of the D and G peaks for PC800 and PC900 fibres, evidenced with a green vertical line, compared to a grey vertical line for the other fibres.

Table 4 | WAXS analysis results and their fits for the manufactured carbon fibres, and comparison with FC and T800 fibres

Fibre type	2θ [°]	FWHM [°]	L_c [nm]	d-spacing [Å]	f_H [–]
T800[60]	25.800	3.898	1.800	3.004	0.910
FC	23.078	4.304	1.618	3.353	0.791
PC800	22.550	6.009	1.161	3.431	0.558
PC900	22.639	5.877	1.187	3.417	0.589
PC1000	22.672	5.655	1.234	3.412	0.605
PC1100	22.721	5.598	1.247	3.405	0.631

Table 5 | Mechanical properties for the partially carbonised carbon fibres and comparison with FC and T800 fibres

Fibre type	Tensile modulus [GPa]	Tensile strength [GPa]	Strain to failure [%]
T800	241.35 ± 3.39	3.85 ± 0.66	1.70 ± 0.27
FC[32]	204.45 ± 7.34	2.81 ± 0.62	1.44 ± 0.31
PC800	65.20 ± 3.42	0.91 ± 0.23	1.43 ± 0.34
PC900	99.46 ± 6.09	1.04 ± 0.25	1.08 ± 0.26
PC1000	120.30 ± 5.86	1.32 ± 0.36	1.15 ± 0.30
PC1100	165.99 ± 6.24	2.23 ± 0.49	1.42 ± 0.30

22.721°, corresponding to interlayer spacings of 3.431–3.405 Å. These values decrease progressively with increasing carbonisation temperature, indicative of gradual turbostratic ordering. Concurrently, the FWHM of the peaks decreases with the same trend, leading to an average crystallite thickness L_c, which is increased from 1.161 nm at 800 °C to 1.247 nm at 1100 °C. From the intensity along the azimuthal direction, Herman's orientation factor (f_H) also increases from 0.558 to 0.631, indicating an enhanced axial alignment of graphitic domains and internal porosity[41]. Further structural development is observed in the FC fibres carbonised at 1300 °C, which exhibits a higher 2θ value (23.078°), reduced interlayer spacing (3.353 Å), larger crystallite size (1.618 nm), and a substantially improved orientation (f_H = 0.791). Nevertheless, this degree of graphitisation remains below that of the commercial T800 reference fibre, characterised by a sharper [002] reflection, larger L_c (1.800 nm), smaller d-spacing (3.004 Å), and the highest orientation factor (f_H = 0.910).

The combined Raman, WAXS, and elemental analysis results indicate a progressive transition from a highly disordered carbonaceous network towards a more ordered turbostratic structure with increasing carbonisation temperature. Raman spectroscopy shows a gradual decrease in the I_D/I_G ratio and a corresponding increase in the estimated crystallite size (L_a), while WAXS analysis reveals an increase in crystallite thickness (L_c), a reduction in interlayer spacing, and an increase in the Herman's orientation factor. Together with the elemental analysis, indicating progressive aromatisation and heteroatom removal, these observations consistently describe the structural evolution of the fibres and provide the basis for interpreting the observed mechanical and electrochemical behaviour, which will be discussed in the following sections.

Mechanical performance

The results from the mechanical testing are presented in Table 5. The mechanical properties of carbon fibres are primarily determined by the tension applied during stabilisation and the maximum carbonisation temperature[42]. Among the samples, the T800 carbon fibre exhibits the best mechanical performance, with strain to failure, tensile strength, and modulus values approximately 10–20% higher than those of the FC fibre. This improvement is likely related to a lower carbonisation temperature, 1300 °C for the FC fibres, while the exact temperature for the T800 fibres is not disclosed. The partially carbonised fibres show significantly lower mechanical performance. The modulus of the PC800 fibre is the lowest, reaching only 20–30% of that of the two IM fibres. However, the modulus increases with the carbonisation temperature, showing a 30 GPa modulus increase per 100 °C increase in carbonisation temperature. A similar trend is observed for the tensile strength. Values around one quarter of those of IM fibres are measured for PC800 fibres, while PC1100 fibres show around 40% lower values. The strain to failure shows values comparable to IM fibres for all partially carbonised fibres.

Mechanical properties are known to be affected by crystallite size and orientation[24,43]. All partially carbonised fibres demonstrate lower mechanical performance in comparison to the IM fibres. This is in agreement with the results from the Raman spectroscopy and the WAXS analyses. An increase in the maximum reached carbonisation temperature leads to larger crystallites and a more ordered microstructure.

Electrochemical performance

Electrochemical cycling is employed to evaluate various electrochemical properties such as the specific capacity, the cycling reversibility and the long-term stability of the active material. The electrochemical performance of FC and T800 fibres was reported not to differ significantly, with less than a 10% difference in the measured capacity[32]. Therefore, in the following part, only T800 fibres are used for the comparison with the partially carbonised fibres. Due to the low electrical conductivity of PC800 fibres, only PC900, PC1000, and PC1100 fibres could be tested for their electrochemical performance.

The results from the electrochemical testing are presented in Table 6. Figure 3a shows the evolution of the specific capacity for various currents for the first 30 cycles. All investigated fibre samples exhibit high reversibility across all applied C-rates. The partially carbonised fibres consistently deliver higher specific capacities compared to the commercial T800 reference fibres. This difference is most pronounced at the lowest C-rate and gradually diminishes with increasing C-rates. Within the group of partially carbonised fibres, the highest first-cycle specific capacities are observed for the fibres carbonised at the lowest carbonisation temperature. However, these higher first-cycle specific capacities are accompanied by larger irreversible capacity losses. In subsequent cycles, fibres produced at higher carbonisation temperatures demonstrate higher specific capacities compared to those

Table 6 | Galvanostatic cycling results for the partially carbonised carbon fibres and comparison with FC and T800 fibres

Fibre type	1st cycle capacity at 0.05 C (used current in mA) [mAh/g]	Reversible capacity at 0.1 C (used current in mA) [mAh/g]	1st cycle loss [%]	50th cycle CE [%]
T800	295 (0.35)	130 (0.70)	31	98.47
PC800[a]	–	–	–	–
PC900	782 (0.73)	184 (1.46)	53	99.49
PC1000	733 (0.80)	215 (1.60)	46	99.65
PC1100	678 (0.72)	240 (1.42)	46	99.86

Coulombic efficiency is defined as the ratio of discharge capacity to charge capacity within the same cycle.
[a]The electrochemical cycling for PC800 fibres could not be performed due to the low electrical conductivity of the material.

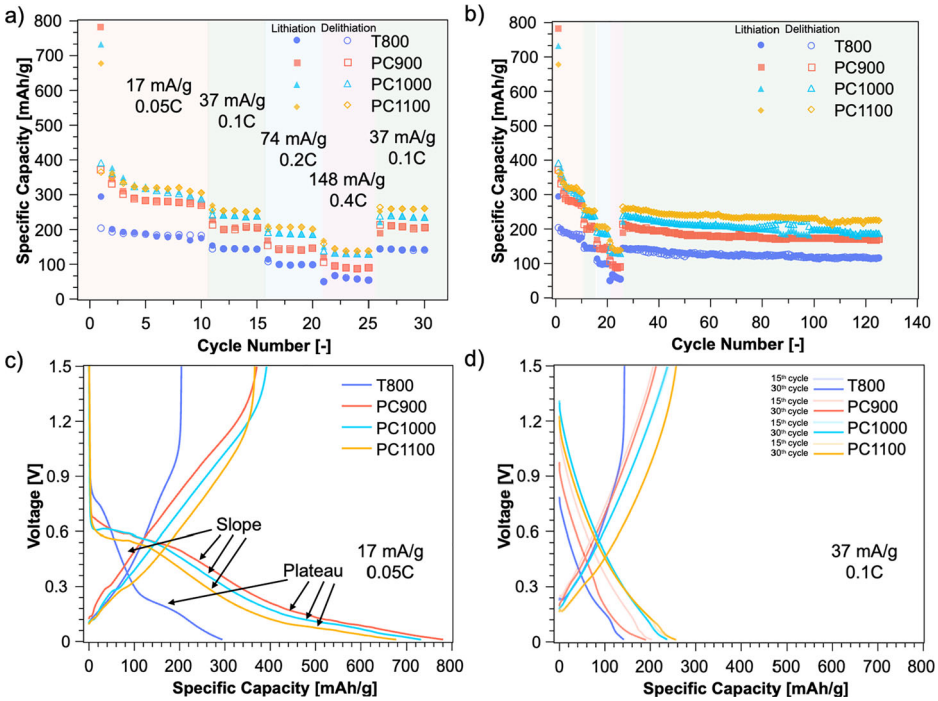

Fig. 3 | Electrochemical cycling results. a Specific capacities for the electrochemical cycling (lithiation and delithiation) at different C-rates for the first 30 cycles. **b** Overall specific capacities for the electrochemical cycling (lithiation and delithiation) at different C-rates for all the cycles up to 125 cycles. **c** Charge/discharge voltage profiles for the 1st cycle at 0.05 C rate. **d** Charge/discharge voltage profiles comparison for the 15th and 30th cycle at 0.1 C rate.

carbonised at lower temperatures. This trend is likely related to differences in the microstructure. As confirmed by the Raman and WAXS analyses, fibres manufactured at lower carbonisation temperatures exhibit smaller crystallites, larger *d*-spacing values, and a more disordered microstructure. While these features facilitate initial lithium insertion, the associated voids and disordered domains trap lithium ions, causing irreversible losses[44,45]. Furthermore, the low electrical conductivity of fibres manufactured at lower carbonisation temperatures would also lead to lower values of lithium storage capacities. For example, from Ohm's law considerations, for cycling at 0.05 C, at a potential of 0.1 V, the critical length for PC900 fibres would be 1.2 cm, well below the electrode length of 4 cm[46]. This phenomenon would be even more significant for the higher C-rates. Figure 3b presents the longer-term cycling behaviour up to 125 cycles. Beyond capacity, the lower electrical conductivity of the partially carbonised fibres also contributes to increased overpotential, particularly at higher C-rates, which explains the observed convergence of capacity values between partially carbonised and T800 fibres with increasing current density (Fig. 3a). These effects are least pronounced for PC1100 fibres, which combine the highest conductivity among the partially carbonised fibres with the highest reversible capacity, making them the most promising candidate for structural battery applications.

All fibre types maintain high Coulombic efficiencies, following the same trends described above. Even after extended cycling, the partially carbonised fibres outperform the T800 reference across all C-rates, achieving up to 40% higher specific capacity.

Figure 3c shows the first cycle voltage profiles for lithiation and delithiation. A conspicuous improvement in first cycle lithiation specific capacity for partially carbonised fibres is evident, as well as a quite different shape for the voltage profile. Due to the differences in the microstructure, direct comparisons of the voltage profiles are complicated. In the initial part of the curves for the lithiation, the solid-electrolyte interphase (SEI) is formed at lower voltages compared to commercially available carbon fibres. Furthermore, the insertion/intercalation of lithium ions in the graphitic domains seems to assume a less pronounced slope for partially carbonised fibre. The slopes for this part of the voltage profiles also seem to be divided into two different regions, one at higher voltages and one at lower voltages. Finally, the plateau region, which is believed to be associated with the insertion of lithium ions into the porosity of the microstructure, is significantly extended for partially carbonised carbon fibres[47–49]. This is likely due to the presence of a higher number of pores in these fibre types. As can be seen in Fig. S2, the difference between the curves is also influenced by the C-rate used: by increasing the C-rate, the voltage profiles for T800 fibres become more like those of partially carbonised fibres, almost overlapping at a specific current of 148 mA g^{-1} (corresponding to 0.4 C rate). In Fig. 3d, the reversibility of the behaviour is further demonstrated. The 15th and 30th cycles overall, performed at a specific current of 37 mA g^{-1} (corresponding

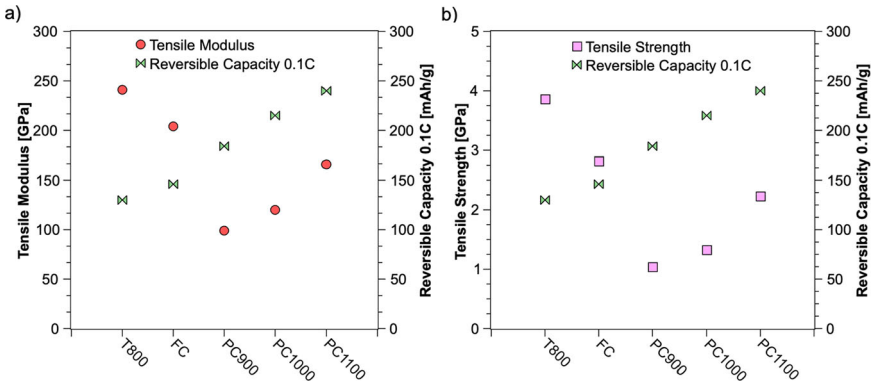

Fig. 4 | Multifunctional performance plots for the fibres characterised in this study. a Tensile modulus and reversible capacity at 0.1 C (50th cycle). **b** Tensile strength and reversible capacity at 0.1 C (50th cycle).

to 0.1 C rate), show an almost perfect overlapping of the curves, indicating reversibility of the lithium insertion/extraction process. Slight differences are only observed for PC900 fibres, most likely due to the more disordered microstructure.

EIS was employed to investigate the interfacial and transport properties of the PC fibre anodes as a function of carbonisation temperature, with Nyquist and Bode plots shown in Fig. S3. The results for the EIS of T800 carbon fibres were reported by Chaudhary and Tavano et al.[30] Equivalent circuit fitting was performed using the circuit $R1 + (Q1\|R2) + Q2$, comprising a series resistance ($R1 = R_s$), a constant phase element (CPE) ($Q1$) in parallel with the charge-transfer resistance ($R2 = R_{ct}$), and a second CPE ($Q2$) in series to describe the low-frequency diffusion response. The Nyquist plots reveal a depressed semicircle in the high-to-mid frequency region for all three samples, followed by a steep low-frequency diffusion tail with angles between 59° and 82° significantly exceeding the 45° characteristic of classical semi-infinite Warburg diffusion, indicative of anomalous sub-diffusion[50]. A CPE element ($Q2$) was therefore used in place of a standard Warburg element to model this response. The ohmic resistance R_s decreased with carbonisation temperature, from 3.87 Ω for PC900 to 2.40 Ω for PC1000 and 1.36 Ω for PC1100, in agreement with the progressive increase in electrical conductivity upon graphitisation and consistent with the reduced ohmic overpotential observed in the galvanostatic cycling data. The depression of the semicircle, quantified by the constant phase element (CPE) exponent n_1, was approximately 0.61, 0.60, and 0.73 for PC900, PC1000, and PC1100, respectively, reflecting significant interfacial heterogeneity consistent with the disordered, partially graphitised microstructure at these carbonisation temperatures. The charge-transfer resistance R_{ct}, extracted from the diameter of the depressed semicircle, was 120.14, 27.27, and 71.99 Ω for PC900, PC1000, and PC1100, respectively. The anomalously low R_{ct} of PC1000 relative to the trend expected across the carbonisation temperature series is attributed to the transient structural state at 1000 °C, where the carbon sits at the transition between amorphous and turbostratic ordering[51]. The diffusion CPE exponent n_2 was comparable across all three samples (0.89, 0.92, and 0.90 for PC900, PC1000, and PC1100), indicating a similarly disordered diffusion environment in all cases, with the low-frequency phase response asymptoting towards ($-n_2 \cdot 90° \approx 80°$) for all three samples. The Bode plots corroborate the impedance trends, showing a systematic decrease in impedance at high frequencies from PC900 to PC1100, consistent with the R_s trend. The semicircle-related phase angle minima, extracted from the fitted model, were −39.9°, −32.2°, and −52.5° for PC900, PC1000, and PC1100, respectively. The shallow minimum of PC1000 relative to the other two samples is consistent with its anomalously low R_{ct}, while the deeper minimum of PC1100 reflects a more capacitively active interface consistent with its higher n_1 value and more ordered carbon microstructure at 1100 °C. The similarities between PC1100 and T800 carbon fibres in terms of R_s (1.66 Ω) and R_{ct} (89.2 Ω) indicate that the microstructure achieved at 1100 °C is relatively close to that of fully carbonised fibres, while the quite significant differences between PC1100 and PC1000 show that a notable microstructural evolution takes place at temperatures around 1000 °C.

The electrochemical results are consistent with previous studies and with the Raman and WAXS analyses[23,31,32]. Earlier research has shown that carbon fibres with a turbostratic microstructure and small crystallite size exhibit lithium storage behaviour comparable to that of amorphous carbon. However, unlike fully amorphous materials, these fibres preserve certain graphitic domains that still allow limited lithium intercalation. According to the so-called "single-layer model," the amorphous regions surrounding the disordered crystalline structures hinder lithium insertion into the graphitic layers. Consequently, lithium ions are predominantly stored within the amorphous domains and at structural defects such as nanocavities. The superior electrochemical performance of the partially carbonised fibres can thus be attributed to their higher content of amorphous regions, increased defect density, greater number of nanocavities, and smaller crystalline domains[24,52–54]. Although disordered carbon domains can provide additional lithium storage sites through defects, edge planes, and nanocavities, the improved electrochemical performance observed at higher carbonisation temperatures cannot be attributed solely to the amorphous regions. Instead, the structural evolution towards more ordered graphitic domains improves electronic conductivity and facilitates reversibility, while the remaining amorphous and defect-rich regions continue to provide accessible lithium storage sites. The electrochemical behaviour therefore results from the interplay between structural ordering and residual disorder within the carbon network.

Conclusion

In this study, partially carbonised carbon fibres were investigated as an alternative to intermediate modulus carbon fibres for structural battery applications. Here, the influence of the carbonisation temperature on the microstructure, mechanical performance, and electrochemical behaviour was systematically examined. Fibres carbonised at the lowest temperature (800 °C) exhibited insufficient electrical conductivity and could not be tested electrochemically. In contrast, fibres carbonised at higher temperatures demonstrated high Coulombic efficiencies (up to 99.86% at the 50th cycle) and consistent capacity retention across 125 cycles. A marked reduction in mechanical performance was observed with decreasing carbonisation temperature, with tensile modulus and tensile strength up to 75% lower than those of IM carbon fibres. However, the electrochemical reversible capacity improved by up to 40% at the lowest C-rates compared to IM fibres. A summary of the multifunctional performance of the investigated fibres is presented in Fig. 4a-and b.

Unlike previous studies that explored processing-property relationships in carbon fibre negative electrodes, this work demonstrates that no trade-off exists between mechanical and electrochemical performance[31,32]. Higher carbonisation temperatures resulted in simultaneous improvements in tensile strength, tensile modulus, and lithium-ion storage capacity. This trend is primarily attributed to microstructural evolution with temperature. The combined structural and compositional analyses provide a mechanistic explanation for the simultaneous evolution of mechanical and electrochemical properties observed in the carbon fibres. Raman spectroscopy and WAXS reveal a progressive increase in graphitic ordering, crystallite size,

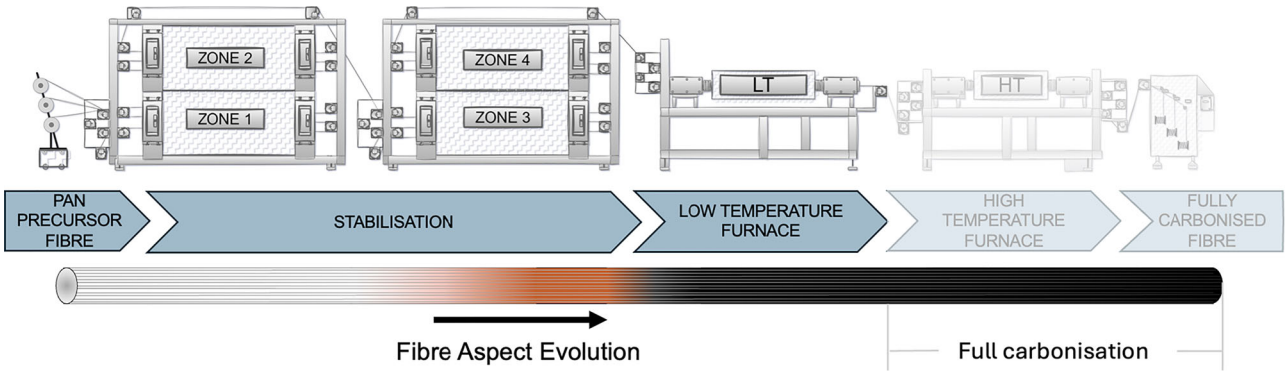

Fig. 5 | Schematic of the research line used for the manufacturing of the partially carbonised fibres. An illustration of the visual aspect change of the fibres along the manufacturing process is also shown.

Table 7 | Different carbonisation temperatures used in the low temperature carbonisation furnace (LT in Fig. 5)

Fibre type	Low temperature oven zone 1 [°C]	Low temperature oven zone 2 [°C]	Low temperature oven zone 3 [°C]	High temperature oven zone 1 [°C]	High temperature oven zone 2 [°C]
FC	284	450	600	1000	1300
PC800	450	650	800	N/A	N/A
PC900	450	700	900	N/A	N/A
PC1000	450	750	1000	N/A	N/A
PC1100	450	800	1100	N/A	N/A

For comparison purposes, the temperatures used for FC fibres are also included[32]. Here, the high-temperature carbonisation furnace was equipped with two distinct zones.

and domain orientation with increasing carbonisation temperature, while elemental analysis indicates the gradual removal of heteroatoms and increased aromatisation of the carbon network. This microstructural evolution enhances load transfer and electrical conductivity through the formation of more ordered graphitic domains, which contribute to the improved mechanical stiffness and strength of the fibres. At the same time, the coexistence of graphitic domains and remaining defect-rich regions provides sites for lithium storage. The results, therefore, suggest that the observed multifunctional performance arises from the interplay between structural ordering and residual disorder within the carbon network.

These findings expand the design space for structural battery composite electrodes, particularly for applications where high electrochemical performance is prioritised over mechanical stiffness. Furthermore, owing to the similarity between partially carbonised fibres and conventional hard carbon materials, this study opens new pathways for exploring alternative chemistries, such as sodium-ion and potassium-ion systems, in structural battery applications. Overall, these results establish clear structure-property relationships across physical, mechanical, and electrochemical domains, providing guidance for tailoring carbon fibre microstructures through controlled carbonisation to meet multifunctional performance targets.

Methods

Materials

Carbon fibres were manufactured at Carbon Nexus, part of the Institute for Frontier Materials at Deakin University (Australia), using a research-grade continuous production line. The process was consistent with previous studies by Xu et al. and Tavano et al.[31,32]. A 24 K polyacrylonitrile (PAN) tow, sourced from Bluestar Ltd (China), served as the precursor. Following stabilisation, carbonisation was performed exclusively in the low-temperature furnace (LT furnace) equipped with three distinct zones, reaching a peak temperature of 1100 °C. The line operated at 30 m h^{-1}, corresponding to residence times of ~2 h during stabilisation and 2.5 min during carbonisation. The applied tension averaged 2300 cN during stabilisation and was adjusted to 1200 cN during carbonisation. Once processed, fibres were collected using a winder. A schematic of the manufacturing process is depicted in Fig. 5. PAN-based T800 carbon fibre tows spread to unidirectional ultrathin tapes (TeXtreme®, T800SC-12k50C) were supplied by Oxeon AB (Sweden). The detailed process temperatures are shown in Table 7. No detailed process temperatures are known for T800 carbon fibres.

Half-cell components included a glass fibre separator (Whatman GF/A, ~260 µm), lithium metal foil (99.9%, 0.75 mm thick), and an electrolyte mixture of LiTFSI (anhydrous, 99.99%), propylene carbonate (PC, ≥99%) and ethylene carbonate (EC, 99%). Glass fibre separators and lithium metal foils were obtained from Sigma-Aldrich (USA). The electrolyte mixture was purchased from Solvionic (France). Copper and nickel foils, along with silver conductive glue, were sourced from Ted Pella, Inc. (USA).

Physical characterisation

Fibre density was measured using an Ultrapyc 1200e pycnometer (Quantachrome, Austria) with three replicates for each fibre type. Fibre diameter was estimated from the density and fibre mass, corroborated with vibrational analysis from a Favimat+ single fibre tensile tester (Textechno, Germany). Electrical conductivity was determined using the four-point probe method with ten replicates for each fibre type. Brunauer–Emmett–Teller (BET) surface area was measured using inverse gas chromatography with octane at 30 °C (Surface Measurement Systems, UK). Surface morphology was examined via a LEO-1550 field-emission scanning electron microscope (Zeiss, Germany). Elemental analysis of the fibre samples was performed using a Vario Macro Cube Elemental Analyser (Elementar, Germany). Two samples of each fibre type, weighing 20–22 mg, were tested. The carbon (C), hydrogen (H), and nitrogen (N) content was measured directly, while the oxygen (O) content was calculated by subtracting the combined wt% of the other elements from 100 wt%.

Microstructural analysis

Raman spectra were collected using a WITec alpha300 R spectrometer equipped with a Zeiss LSM confocal microscope and a ×50 objective (NA = 0.75). Measurements were performed at room temperature (23 °C) using a 532 nm excitation laser focused to ~300 nm. Spectra were recorded in backscattering geometry using a 100 µm slit and a 600 lines mm^{-1} grating.

A CCD detector captured the signal, with each spectrum composed of 60 accumulations (1 s exposure each). Data were processed in WITec Project FIVE software using baseline subtraction and Savitzky–Golay smoothing. Peak fitting was performed with Lorentzian profiles, and the spectra were normalised to the most intense peak. Using the Tuinstra–Koenig relation (TK), the average crystallite length (L_a) was estimated based on the I_D/I_G intensity ratios[39]. The average crystallite length was also calculated using another relation proposed by Mallet-Ladeira (ML)[40]. In this case, the average crystallite length is calculated from the HWHM of the G peak.

Wide-angle X-ray scattering (WAXS) measurements were carried out at the Institute for Frontier Materials, Deakin University (Australia), using a Xeuss 3.0 system operating with an X-ray beam energy of 9 keV. The sample-to-detector distance was set to 60 mm, and each exposure lasted 360 s. Carbon fibre samples were vertically mounted on a 3D-printed holder and aligned perpendicular to the incident beam. For each fibre type, the fibre bundles were scanned at three different positions. The holder was mounted on an X–Y linear stage within a vacuum chamber, allowing precise positioning. Scattering patterns collected along the equatorial direction were integrated over an azimuthal angle of ±2° and converted into X–Y plots of X-ray intensity versus scattering angle (2θ). Peaks in the resulting plots were fitted using a pseudo-Voigt function[55], and the full width at half maximum (FWHM) of the fitted peaks was used to calculate the crystallite size L_c via Scherrer's equation[56]. Peak positions were used to determine lattice spacing (d) according to Bragg's law[57]. To assess crystallite orientation, scattering patterns along the azimuthal direction were analysed. These were converted into intensity versus azimuthal angle (φ) plots, and the peaks were fitted with a Gaussian function. The FWHM of these fits was used to quantify Herman's orientation factor (f_H)[58].

Mechanical characterisation

Tensile strength, elastic modulus, and strain to failure were determined through single filament testing on a Favimat+ machine (Textechno, Germany), using a 210 cN load cell and a 20 mm gauge length, according to ASTM D3822-07. A total of 75 fibres per type were tested at a constant strain rate of 1 mm min^{-1}.

Electrochemical characterisation

For electrochemical measurements, 24K carbon fibre tows were split into two fictitious 12K bundles. Electrical contact was established by bonding copper current collectors to the fibres using silver paint. The assembled electrodes were vacuum-dried at 50 °C overnight and transferred to an argon-filled glovebox (H_2O and O_2 <1 ppm). Pouch cells were assembled using the carbon fibre electrode and lithium metal as both counter and reference electrodes, with a nickel current collector. The two electrodes were separated by a glass microfiber separator. A 1.0 M LiTFSI in EC:PC solution was used as electrolyte. After electrolyte addition, the cells were vacuum-sealed. Galvanostatic cycling was conducted on a Neware CT-4008-5V10mA-164 battery cycler (Neware, China) within a voltage range of 0.01–1.50 V vs. Li/Li^+. Current densities were based on the theoretical capacity of graphite (372 mAh g^{-1}), beginning with 10 cycles at 0.05 C, followed by 5 cycles each at 0.1, 0.2, and 0.4 C, and concluding with 100 cycles at 0.1 C. A 1-h rest was applied after each charge/discharge cycle. Electrochemical Impedance Spectroscopy (EIS) was conducted using a Gamry Interface 1010B potentiostat (Gamry, USA) with a frequency range between 160 mHz and 20 kHz, and an AC perturbation amplitude of 10 mV.

Data availability

The datasets generated and/or analysed during the current study are available from the corresponding authors upon reasonable request.

Received: 23 January 2026; Accepted: 8 May 2026;
Published online: 22 May 2026

References

1. Aubin, C. A. et al. Towards enduring autonomous robots via embodied energy. *Nature* **602**, 393–402 (2022).
2. Jin, T., Singer, G., Liang, K. & Yang, Y. Structural batteries: advances, challenges and perspectives. *Mater. Today* **62**, 151–167 (2023).
3. Hopkins, B. J., Long, J. W., Rolison, D. R. & Parker, J. F. High-performance structural batteries. *Joule* **4**, 2240–2243 (2020).
4. Asp, L. E. & Greenhalgh, E. S. Structural power composites. *Compos. Sci. Technol.* **101**, 41–61 (2014).
5. Asp, L. E., Johansson, M., Lindbergh, G., Xu, J. & Zenkert, D. Structural battery composites: a review. *Funct. Compos. Struct.* **1**, 042001 (2019).
6. Johannisson, W., Zenkert, D. & Lindbergh, G. Model of a structural battery and its potential for system level mass savings. *Multifunct. Mater.* **2**, 035002 (2019).
7. Meng, C. et al. Multifunctional structural ultrabattery composite. *Nano Lett.* **18**, 7761–7768 (2018).
8. Moyer, K. et al. Carbon fiber reinforced structural lithium-ion battery composite: multifunctional power integration for CubeSats. *Energy Storage Mater.* **24**, 676–681 (2020).
9. Greenhalgh, E. S. et al. Characterization and reporting protocols for structural power composites: a perspective. *Adv. Energy Mater.* **15**, e04702 (2025).
10. Cattaruzza, M. et al. Hybrid polymer–liquid lithium ion electrolytes: effect of porosity on the ionic and molecular mobility. *J. Mater. Chem. A* **11**, 7006–7015 (2023).
11. Ihrner, N., Johannisson, W., Sieland, F., Zenkert, D. & Johansson, M. Structural lithium ion battery electrolytes via reaction induced phase-separation. *J. Mater. Chem. A* **5**, 25652–25659 (2017).
12. Schneider, L. M., Ihrner, N., Zenkert, D. & Johansson, M. Bicontinuous electrolytes via thermally initiated polymerization for structural lithium ion batteries. *ACS Appl. Energy Mater.* **2**, 4362–4369 (2019).
13. Larsson, C., Larsson, F., Xu, J., Runesson, K. & Asp, L. E. Effects of lithium insertion induced swelling of a structural battery negative electrode. *Compos. Sci. Technol.* **244**, 110299 (2023).
14. Tavano, R. et al. Mechanical characterisation of a structural battery electrolyte. *Polymer* **312**, 127646 (2024).
15. Randall, J. D. et al. Assessing virgin and reclaimed carbon fibre electrodes in structural batteries. *Chem. Eng. J.* 166504 https://doi.org/10.1016/j.cej.2025.166504 (2025).
16. Ruland, W. Carbon fibers. *Adv. Mater.* **2**, 528–536 (1990).
17. Snyder, J. F., Wong, E. L. & Hubbard, C. W. Evaluation of commercially available carbon fibers, fabrics, and papers for potential use in multifunctional energy storage applications. *J. Electrochem. Soc.* **156**, A215 (2009).
18. Jacques, E. et al. Impact of electrochemical cycling on the tensile properties of carbon fibres for structural lithium-ion composite batteries. *Compos. Sci. Technol.* **72**, 792–798 (2012).
19. Jacques, E., Hellqvist Kjell, M., Zenkert, D., Lindbergh, G. & Behm, M. Expansion of carbon fibres induced by lithium intercalation for structural electrode applications. *Carbon* **59**, 246–254 (2013).
20. Jacques, E., Kjell, M. H., Zenkert, D. & Lindbergh, G. The effect of lithium-intercalation on the mechanical properties of carbon fibres. *Carbon* **68**, 725–733 (2014).
21. Duan, S. et al. Effect of lithiation on the elastic moduli of carbon fibres. *Carbon* **185**, 234–241 (2021).
22. Kjell, M. H., Jacques, E., Zenkert, D., Behm, M. & Lindbergh, G. PAN-based carbon fiber negative electrodes for structural lithium-ion batteries. *J. Electrochem. Soc.* **158**, A1455 (2011).
23. Hagberg, J., Leijonmarck, S. & Lindbergh, G. High precision coulometry of commercial PAN-based carbon fibers as electrodes in structural batteries. *J. Electrochem. Soc.* **163**, A1790 (2016).
24. Fredi, G. et al. Graphitic microstructure and performance of carbon fibre Li-ion structural battery electrodes. *Multifunct. Mater.* **1**, 015003 (2018).

25. Johansen, M., Schlueter, C., Tam, P. L., Asp, L. E. & Liu, F. Mapping nitrogen heteroatoms in carbon fibres using atom probe tomography and photoelectron spectroscopy. *Carbon* **179**, 20–27 (2021).
26. Asp, L. E. et al. A structural battery and its multifunctional performance. *Adv. Energy Sustain. Res.* **2**, 2000093 (2021).
27. Chaudhary, R., Chetry, A., Xu, J., Xia, Z. & Asp, L. E. Structural positive electrodes engineered for multifunctionality. *Adv. Sci.* **11**, 2404012 (2024).
28. Chaudhary, R., Xu, J., Xia, Z. & Asp, L. E. Unveiling the multifunctional carbon fiber structural battery. *Adv. Mater.* **36**, 2409725 (2024).
29. Yang, T., Zhao, Y., Liu, H. & Xiong, S. Effect of sizing agents on surface properties of T800 grade CF and thermal aging time on mechanical properties of T800 grade CF/epoxy composites. *Int. J. Polym. Sci.* **2021**, 4562560 (2021).
30. Chaudhary, R., Tavano, R., Xu, J. & Asp, L. E. Lithium-ion transport in carbon fibers for structural batteries. *Adv. Energy Sustain. Res.* **7**, e202500377 (2026).
31. Xu, J. et al. Effect of tension during stabilization on carbon fiber multifunctionality for structural battery composites. *Carbon* **209**, 117982 (2023).
32. Tavano, R. et al. Influence of carbonisation temperatures on multifunctional properties of carbon fibres for structural battery applications. *Batter. Supercaps* **7**, e202400110 (2024).
33. Zhou, Z. et al. Synergistic catalytic conversion of polysulfide from Janus N-CNTs/Ni@CoS2 nanocrystals for advanced lithium–sulfur battery. *Mater. Today Chem.* **52**, 103387 (2026).
34. Guo, X. et al. Multicomponent synergistic Janus separator enabling rapid polysulfide conversion and free lithium dendrite for advanced lithium-sulfur batteries. *Chem. Eng. J.* **529**, 172604 (2026).
35. Peng, X. et al. Co-NC/Nb2O5 heterostructure enable the synergistic fast sulfur redox kinetics and uniform lithium deposition for advanced lithium sulfur batteries. *J. Colloid Interface Sci.* **700**, 138455 (2025).
36. Ding, J., Ji, D., Yue, Y. & Smedskjaer, M. M. Amorphous materials for lithium-ion and post-lithium-ion batteries. *Small* **20**, 2304270 (2024).
37. Xu, J. et al. Characterization of the adhesive properties between structural battery electrolytes and carbon fibers. *Compos. Sci. Technol.* **188**, 107962 (2020).
38. Melanitis, N., Tetlow, P. L. & Galiotis, C. Characterization of PAN-based carbon fibres with laser Raman spectroscopy: Part I Effect of processing variables on Raman band profiles. *J. Mater. Sci.* **31**, 851–860 (1996).
39. Tuinstra, F. & Koenig, J. L. Raman spectrum of graphite. *J. Chem. Phys.* **53**, 1126–1130 (1970).
40. Mallet-Ladeira, P. et al. A Raman study to obtain crystallite size of carbon materials: a better alternative to the Tuinstra–Koenig law. *Carbon* **80**, 629–639 (2014).
41. Li, X. et al. WAXD/SAXS study and 2D fitting (SAXS) of the microstructural evolution of PAN-based carbon fibers during the pre-oxidation and carbonization process. *New Carbon Mater* **32**, 130–136 (2017).
42. Park, S.-J. Precursors and manufacturing of carbon Fibers. In *Carbon Fibers* (ed. Park, S.-J.) 31–67 (Springer, 2018).
43. Johnson, D. J. Structure-property relationships in carbon fibres. *J. Phys. Appl. Phys.* **20**, 286–291 (1987).
44. Stevens, D. A. & Dahn, J. R. The mechanisms of lithium and sodium insertion in carbon materials. *J. Electrochem. Soc.* **148**, A803 (2001).
45. Johansen, M. et al. Unravelling lithium distribution in carbon fibre electrodes for structural batteries with atom probe tomography. *Carbon* **225**, 119091 (2024).
46. Millikan, A. R. *Elements of Electricity: A Practical Discussion of the Fundamental Laws and Phenomena of Electricity and their Practical Applications in the Business and Industrial World* (American Technical Society, 1917).
47. Yang, G. et al. Insights into lithium and sodium storage in porous carbon. *Nano Lett.* **20**, 3836–3843 (2020).
48. Saju, S. K. et al. Hard carbon anode for lithium-, sodium-, and potassium-ion batteries: advancement and future perspective. *Cell Rep. Phys. Sci.* **5**, 101851 (2024).
49. Fujimoto, H., Tokumitsu, K., Mabuchi, A., Chinnasamy, N. & Kasuh, T. The anode performance of the hard carbon for the lithium ion battery derived from the oxygen-containing aromatic precursors. *J. Power Sources* **195**, 7452–7456 (2010).
50. Lazanas, A. & Prodromidis, M. Electrochemical Impedance Spectroscopy—A Tutorial, *ACS Meas. Sci. Au* **3**, 162–193 (2023).
51. Erol, S. & Orazem, M. E. The influence of anomalous diffusion on the impedance response of LiCoO2|C batteries. *J. Power Sources* **293**, 57–64 (2015).
52. Endo, M., Nishimura, Y., Takahashi, T., Takeuchi, K. & Dresselhaus, M. S. Lithium storage behavior for various kinds of carbon anodes in Li ion secondary battery. *J. Phys. Chem. Solids* **57**, 725–728 (1996).
53. Endo, M. & Kim, Y. A. Applications of advanced carbon materials to the lithium ion secondary battery. In *Carbon Alloys* (eds Yasuda, E. et al.) Ch. 25, 417–433 (Elsevier Science, 2003).
54. Endo, M. et al. In situ Raman study of PPP-based disordered carbon as an anode in a Li ion battery. *Synth. Met.* **98**, 17–24 (1998).
55. Gibaud, A. & Hazra, S. X-ray reflectivity and diffuse scattering. *Curr. Sci.* **78**, 1467–1477 (2000).
56. Nunna, S. et al. Investigation of progress of reactions and evolution of radial heterogeneity in the initial stage of thermal stabilization of PAN precursor fibres. *Polym. Degrad. Stab.* **125**, 105–114 (2016).
57. Le Pevelen, D. D. Small molecule X-ray crystallography, theory and workflow. In *Encyclopedia of Spectroscopy and Spectrometry* 2nd edn (ed. Lindon, J. C.) 2559–2576 (Academic Press, 2010).
58. Wilchinsky, Z. W. Measurement of orientation in polypropylene film. *J. Appl. Phys.* **31**, 1969–1972 (1960).
59. Toray. *T800S-Technical Data Sheet-1* https://www.toraycma.com/wp-content/uploads/T800S-Technical-Data-Sheet-1.pdf (2010).
60. Cui, Y. et al. Research on improving the pre-oxidation process of the excellent mechanical strength carbon fiber. *Macromol. Chem. Phys.* **224**, 2300114 (2023).

Acknowledgements

The authors would like to thank the following funding agencies for funding this research: United States Air Force (USAF), USA, Award Number FA8655-21-1-7038, Office of Naval Research (ONR), USA, Award Numbers N62909-22-1-2037 and N62909-22-1-2052. The authors also gratefully acknowledge the financial support from Chalmers' Areas of Advanced Production and Energy and an IM Fellowship (IM230100048) for L.H. This work was partly performed at the Chalmers Material Analysis Laboratory (CMAL). The authors would also like to thank Mr. John Herron, Dr. Maxime Maghe and Mr. Scott Anderson at Carbon Nexus for manufacturing the carbon fibres analysed in the current study.

Author contributions

Ruben Tavano: Writing—original draft, methodology, investigation, formal analysis, conceptualisation, data curation; James D. Randall: Writing—original draft, methodology, investigation, formal analysis, data curation; Nguyen Nguyen Le Thao: Methodology, investigation, formal analysis, and data curation; Claudia Creighton: Writing—original draft, methodology, investigation, formal analysis, data curation; Johanna Xu: Writing—original draft, methodology, investigation, formal analysis; Luke C. Henderson: Writing—original draft, supervision, methodology, funding acquisition, project administration; Leif E. Asp: Writing— original draft, supervision, methodology, funding acquisition and project administration.

Funding

Open access funding provided by Chalmers University of Technology.

Competing interests
The authors declare no competing interests.

Additional information
Supplementary information The online version contains supplementary material available at https://doi.org/10.1038/s43246-026-01194-x.

Correspondence and requests for materials should be addressed to Ruben Tavano or Leif E. Asp.

Peer review information *Communications Materials* thanks the anonymous reviewers for their contribution to the peer review of this work.

Reprints and permissions information is available at http://www.nature.com/reprints

Publisher's note Springer Nature remains neutral with regard to jurisdictional claims in published maps and institutional affiliations.

Open Access This article is licensed under a Creative Commons Attribution 4.0 International License, which permits use, sharing, adaptation, distribution and reproduction in any medium or format, as long as you give appropriate credit to the original author(s) and the source, provide a link to the Creative Commons licence, and indicate if changes were made. The images or other third party material in this article are included in the article's Creative Commons licence, unless indicated otherwise in a credit line to the material. If material is not included in the article's Creative Commons licence and your intended use is not permitted by statutory regulation or exceeds the permitted use, you will need to obtain permission directly from the copyright holder. To view a copy of this licence, visit http://creativecommons.org/licenses/by/4.0/.

© The Author(s) 2026